Published in final edited form as:

Mol Imaging Biol. 2024 June ; 26(3): 503–510. doi:10.1007/s11307-023-01860-3.

Imaging Reactive Oxygen Radicals in Excised Mouse Lung Trapped by Reaction with Hydroxylamine Probes Using 1 GHz Rapid Scan Electron Paramagnetic Resonance

Hanan B. Elajaili[1], **Lukas B. Woodcock**[2], **Tanden A. Hovey**[2], **George A. Rinard**[2], **Samuel DeGraw**[2], **Autumn Canny**[2], **Nathan M. Dee**[1], **Joseph P. Y. Kao**[3], **Eva S. Nozik**[1], **Sandra S. Eaton**[2], **Gareth R. Eaton**[2]

[1]Cardiovascular Pulmonary Research Laboratories and Pediatric Critical Care Medicine, University of Colorado Anschutz Medical Campus, 12700 E. 19th Ave., B131, Aurora, CO 80045, USA

[2]Department of Chemistry and Biochemistry, University of Denver, Denver, CO 80210, USA

[3]Center for Biomedical Engineering and Technology and Department of Physiology, University of Maryland School of Medicine, Baltimore, MD, USA

Abstract

Purpose—Oxidative stress is proposed to be critical in acute lung disease, but methods to monitor radicals in lungs are lacking. Our goal is to develop low-frequency electron paramagnetic resonance (EPR) methods to monitor radicals that contribute to the disease.

Procedures—Free radicals generated in a lipopolysaccharide-induced mouse model of acute respiratory distress syndrome reacted with cyclic hydroxylamines CPH (1-hydroxy-3-carboxy-2,2,5,5-tetramethylpyrrolidine hydrochloride) and DCP-AM-H (4-acetoxymethoxycarbonyl-1-hydroxy-2,2,5,5-tetramethylpyrrolidine-3-carboxylic acid), which were converted into the corresponding nitroxide radicals, CP• and DCP•. The EPR signals of the nitroxide radicals in excised lungs were imaged with a 1 GHz EPR spectrometer/imager that employs rapid scan technology.

✉Gareth R. Eaton, Gareth.eaton@du.edu.

Hanan B. Elajaili and Lukas B. Woodcock contributed equally to this work.

Dedicated to Samuel DeGraw who passed away during the preparation of the study

Author Contributions Elajaili, Hanan B: designed and performed mouse experiments, analyzed data, interpreted results, and wrote manuscript. Woodcock, Lukas B: designed, modified, and tested imager; performed mouse imaging experiments; analyzed data; interpreted results; and wrote manuscript. Hovey, Tanden A.: designed, modified, and tested imager; performed mouse imaging experiments; analyzed data; interpreted results; and wrote manuscript. Rinard, George A.: modified imager and designed performance tests, designed and built rapid scan resonator, and edited manuscript. DeGraw, Samuel: designed and implemented method of automated fitting of nitroxide spectra. Canny, Autumn: designed and implemented software for analyzing spectra of probes in lung, analyzed data, edited manuscript. Nathan, Dee M.: performed mouse experiment and edited manuscript. Kao, Joseph P. Y.: designed spin probe experiments, interpreted results, and edited manuscript. Nozik, Eva S.: designed experiments, interpreted results, and edited manuscript. Eaton, Sandra S.: designed experiments, analyzed data, interpreted results, and wrote manuscript. Eaton, Gareth R.: improved imager, designed experiments, analyzed data, interpreted results, and wrote manuscript. All authors (except for DeGraw) reviewed the final manuscript and approved submission.

Supplementary Information The online version contains supplementary material available at https://doi.org/10.1007/s11307-023-01860-3.

Conflict of Interest The authors declare no competing interests.

Results—The small numbers of nitroxides formed by reaction of the hydroxylamine with superoxide result in low signal-to-noise in the spectra and images. However, since the spectral properties of the nitroxides are known, we can use prior knowledge of the line shape and hyperfine splitting to fit the noisy data, yielding well-defined spectra and images. Two-dimensional spectral-spatial images are shown for lung samples containing $(4.5 \pm 0.5) \times 10^{14}$ CP• and $(9.9 \pm 1.0) \times 10^{14}$ DCP• nitroxide spins. These results suggest that a probe that accumulates in cells gives a stronger nitroxide signal than a probe that is more easily washed out of cells.

Conclusion—The nitroxide radicals in excised mouse lungs formed by reaction with hydroxylamine probes CPH and DCP-AM-H can be imaged at 1 GHz.

Keywords

Acute respiratory distress syndrome; Superoxide; Spin probe; Nitroxide; Rapid scan electron paramagnetic resonance

Introduction

Acute respiratory distress syndrome (ARDS), the most severe form of acute lung injury (ALI), is a principal cause of life-threatening illness in adults and children [1–3]. There is evidence that oxidative stress is critical in pathogenesis of ARDS, but effective methods for monitoring radicals in the lung are lacking. There is urgent need to develop methods that can distinguish between hypo-inflammatory and hyper-inflammatory subphenotypes of ARDS patients who may respond differently to therapies [4–7]. Elajaili et al. reported X-band electron paramagnetic resonance (EPR) spectra of excised lung tissue from mice treated with lipopolysaccharide (LPS) [8]. LPS, a major component of the outer membranes of Gram-negative bacteria, has been used to induce ALI/ARDS. ROS subsequent to LPS exposure is predominantly generated through NADPH oxidase following activation of toll-like receptor 4 [9–12]. Since a long-term goal is monitoring the response of ARDS to treatment, we are developing methods for *in vivo* EPR imaging of radicals at low microwave frequencies. The 1 GHz microwave frequency is chosen as a compromise between depth of penetration in the mouse (deeper at lower frequencies) and sensitivity (greater at higher frequencies). The present paper reports the first steps toward imaging of the radicals involved in ARDS, by imaging of mouse lungs excised after treatment with LPS. To incorporate a spectral dimension in magnetic resonance imaging 2D spectral-spatial imaging was introduced by Lauterbur and co-workers in NMR in 1985 [13] and by Eaton and co-workers in EPR in 1987 [14, 15]. For all imaging modalities feasibility is strongly dependent on adequate signal intensity per voxel. To demonstrate feasibility of EPR imaging of radicals trapped in lung tissue, we now report 2D spectral-spatial images for excised lungs. We use rapid scan EPR as the detection modality because it increases signal-to-noise relative to the more common field-modulated phase-sensitive detected continuous wave (CW) EPR [16].

Our early development of spectral-spatial imaging focused on imaging unknown signals or mixtures of signals, so no assumption was made about the line shapes or number of lines in the spectra [15, 17]. In the present study, we take a different approach to maximize the sensitivity of the measurement. We use the chemical knowledge that LPS-induced superoxide reacts with a cyclic hydroxylamine probe and converts it into a well-

characterized nitroxide radical. Therefore, we know that the EPR signals to be imaged for natural abundance (^{14}N) nitroxides are 3-line spectra with mixed Lorentzian/Gaussian line shapes with 45.2 MHz separation.

Materials and Methods

Mouse Model

Animal studies were approved by the University of Colorado Denver (Aurora, CO) Institutional Animal Care and Use Committee. We used 8–12-weeks-old male and female C57BL/6 mice. There were 4 males and 7 females in the CPH group and 6 males and 9 females in the DCP-AM-H group (Fig. S1).

Injury Model

Lung injury was induced with a single dose of intraperitoneal (IP) lipopolysaccharide (LPS) (*E. coli* O55; Sigma) (10 mg/kg). Mice were treated with LPS [8] and evaluated at 24 h. After delivering the probes *in vivo* to live mice, the mice were euthanized with CO_2 and cervical dislocation. The chest cavity was opened and blood in the lungs was flushed out with 5 mL of cold phosphate-buffered saline (PBS) via the right ventricle. Lungs were excised and kept on ice until the EPR measurements were performed as described below.

Selection of Molecular Probes

Since the goal is detection of the short-lived superoxide radical, we take advantage of cyclic hydroxylamines, a class of EPR molecular probes that react rapidly with superoxide and generate a more stable nitroxide radical with a typical 3-line spectrum that can be detected and quantified by rapid scan EPR imaging. Cyclic hydroxylamines 1-hydroxy-3-carboxy-2,2,5,5-tetramethylpyrrolidine hydrochloride (CPH) (Enzo Life Sciences, Farmingdale, NY) or 4-acetoxymethoxycarbonyl-1-hydroxy-2,2,5,5-tetramethylpyrrolidine-3-carboxylic acid (DCP-AM-H) (gift of Igor Kirilyuk, Novosibirsk Institute of Organic Chemistry, Russia) [18] were used in this study (Fig. 1). To decrease spontaneous oxidation, stock solutions of cyclic hydroxylamines were prepared in Krebs-Henseleit buffer containing 25 μM deferoxamine mesylate salt and 5 μM sodium diethyldithiocarbamate (Sigma Aldrich) and bubbled with nitrogen for 30 min to remove dissolved oxygen. The concentrations of the stock solutions were 18 mM for CPH and 2.5 mM for DCP-AM-H. The stock solutions were prepared fresh daily and kept on ice.

Delivery of Spin Probes

The probes CPH and DCP-AM-H were delivered 24 h after administering LPS treatment to mice. Mice were anesthetized with isoflurane (1–3%), and the probes were administered intratracheally (IT); dosing was 100 μL of 18 mM CPH or 100 μL of 2.5 mM DCP-AM-H. Lungs were harvested surgically 5 min after IT delivery. Lungs were kept on ice, and EPR measurements were performed within 2 to 4 h after the harvest (Fig. S2). For a series of experiments, probe administrations were staggered, and imaging experiments were performed in the same sequence as lung harvesting to achieve approximately the same elapsed time between treatment and EPR measurements. The time between lung harvest and imaging was not correlated with signal intensity (Fig. S2). When warmed to room

temperature, the nitroxide signal decreased appreciably over the course of about an hour, presumably owing to bioreduction. EPR spectroscopy and imaging at L-band were typically completed within ~ 10 min after taking each lung off ice.

Rapid Scan EPR Imaging of the Lung

The L-band (1 GHz) imager is a modification of the 700 MHz imager previously described [19], which was designed to perform either pulse or rapid scan experiments. The 1-GHz bridge was customized for rapid scan and components in the detection path that are not required for rapid scan were removed. These changes decrease losses and hence decrease the noise factor (NF) of the spectrometer, which improves the signal-to-noise of acquired spectra. The first stage of the signal detection path was a low-noise (NF = 0.38) 17 dB gain microwave amplifier which helps set the noise floor for the instrument. The output of a quadrature mixer was amplified by the video amplifier described in Buchanan et al. [19]. Engineering details of the spectrometer/imager and the resonator will be published separately. L-band rapid scan spectra and images are analyzed using MATLAB software (MathWorks, Natick, MA) and EasySpin fitting routines [20].

The reflection resonator used for the imaging experiments is constructed with fine wire to minimize eddy currents induced by the rapidly-scanning magnetic field, as described for rapid scan resonators in ref. [21]. It is 9 mm in diameter and 10-mm long. The resonator Q with sample is about 42, and the efficiency is 0.051 ± 0.002 mT/√W. The sample region in this resonator is perpendicular to the magnet field and is about 8 mm long. Both lungs from a mouse were placed in an NMR tube (8-mm o.d., 7-mm i.d.) that was inserted into the rapid scan resonator. The lossy sample impacts the tuning of the resonator, which was adjusted for each sample. The sinusoidal rapid scan frequency was 26.8 kHz. The sweep widths were calibrated by comparison of the nitrogen hyperfine splitting (A_N) with the known values of 67.1 MHz for ^{15}N-tempol, or 45.2 MHz for CP• and DCP• and were in the range of 5.0 to 5.5 mT. The microwave power was selected to be in the linear response regime, which was a B_1 of about 6.5 μT. A non-gradient spectrum was acquired for spin quantitation. For the images, 11 projections were acquired with equally spaced gradients and a maximum gradient of 1 mT/cm; 2×10^5 scans were summed in 30 s for each projection. With a maximum gradient of 1 mT/cm and nitroxide linewidths of about 0.1 mT, the spatial resolution is about 1 mm. Rapid scan deconvolution was performed using our published procedure [22]. Images were reconstructed as previously described [23].

Spin Quantitation

A standard sample of 1.0 mM ^{15}N,d_{17}-tempol (^{15}N-perdeuterated 4-hydroxy-2,2,6,6-tetramethyl-piperidin-1-oxyl) was prepared gravimetrically and the concentration was confirmed using the spincount software on a Bruker EMXnano. The L-band spectrum of the standard solution in an 8-mm tube was recorded under the same parameters as for the lung samples. The calibration followed literature procedures [24].

The following fitting procedure was used to determine the intensity of the signal for the standard sample, a non-gradient spectrum, or a spectral slice through an image. A reference spectrum for the appropriate nitroxide was calculated with the EasySpin garlic function

using g = 2.006, the experimental operating frequency, the known A_N, two sets of ^{13}C sidebands with A = 14.25 or 17.25 MHz, and a linewidth comprised of 0.1 mT Gaussian and 0.055 mT Lorentzian components. The amplitude of the reference spectrum was matched to that of the experimental spectrum using the EasySpin rescale routine. A cursor was used to select the centers of the 3 windows encompassing the nitrogen (^{14}N) hyperfine lines as shown in Fig. 2; for ^{15}N-nitroxides, there are two windows. The rescale routine was applied only within the 3 (or 2) windows. The width of the window is user-selectable. Limiting the fitting to the windows centered on the peaks decreases the impact of noise on the scaling routine. The rescale routine outputs a scaling factor that is proportional to signal amplitude. The integral of the simulated spectrum, after multiplication by the scaling factor, is proportional to the number of spins. The relationship between integral and absolute number of spins is defined by the results for the standard sample. In the finished displays of the spectral-spatial images, the spatial slices are scaled versions of the spectra calculated to fit the experimental data, and the amplitude is proportional to the spins per mm along the direction of the gradient.

Results

The aim of the experiments was to use rapid scan EPR spectral-spatial imaging to monitor cellular and mitochondrial superoxide production in the lungs of LPS-treated mice. Cellular superoxide was monitored with the hydrophilic CPH probe, which can passively distribute across cell membranes, and the more lipophilic DCP-AM-H probe, which can permeate through cell membranes, be cleaved by cellular esterases, and become trapped intracellularly as a dianion. These probes do not have an EPR signal, but react with superoxide to form persistent nitroxide radicals (Fig. 1). CPH forms CP•. The more lipophilic DCP-AM-H crosses cell membranes, and, once inside the cell, intracellular esterases cleave the acetoxymethyl (AM) ester to unmask a second carboxyl group [18]. Therefore, DCP-AM-H, upon reaction with superoxide and cleavage by esterase, yields DCP•. Because DCP• is a dianion at physiologic pH, it cannot easily cross the cell membrane and exit the cell. Owing to its intracellular localization and the fact that mitochondria are the predominant source of superoxide, intracellular DCP• is primarily attributable to mitochondria [18]. Both CP• and DCP• exhibit characteristic EPR spectra that are easily measurable.

Figure 3 shows an image of the CP• signal in the lungs from an LPS-treated mouse in the sample holder used for EPR imaging. The lungs were oriented such that the magnetic field gradient across the two lungs was as sketched in Fig. 3. Also shown in Fig. 3 is the 2D spectral-spatial image displaying the full EPR lineshape as a function of position along an axis defined by the direction of the gradient. Since there is a single spatial dimension in the image, the spatial profile is determined primarily by the geometry of the tube, which has maximum cross section (and therefore maximum signal amplitude) at the center of the tube where the lungs are closely packed together, so a separation between signals from the two lungs is not observed. The three lines of the ^{14}N nitroxide are displayed on the magnetic field (spectral) axis. The use of spectral fitting eliminates noise in the background. There was no indication in the experimental data of any signals other than those from the nitroxide.

A spectral-spatial image of DCP• in the lungs of an LPS-treated mouse is shown in Fig. 4 for a sample with $(4.5 \pm 0.5) \times 10^{14}$ nitroxide spins. The spectral slices exhibit the characteristic 3-line spectrum of the CP• that was formed by reaction of CPH with superoxide. The signal from the trapped radical extends across both lungs. For a mouse treated with DCP-AM-H, an image acquired with the same parameters as for DCP• is shown in Fig. 4. For these two mice, although the dose of CPH was about 7 times the dose for DCP-AM-H, the intensity of the signal for DCP• was about twice the CP• signal. For the series of LPS-treated mice studied, the average number of nitroxide spins detected for CP• was $(4.5 \pm 1.7) \times 10^{14}$ and for DCP was $(1.2 \pm 0.7) \times 10^{15}$ (Fig. S1). In the related X-band methodology development studies, the dose for CPH was about 4 times as large as for DCP-AM-H, and the concentrations of DCP• was about three times as large as for CP• [8].

Discussion

X-band EPR of slices of lung tissue were used to develop and calibrate the protocol for LPS-treatment of mice [8]. Based on the X-band results, we applied the protocol described above to imaging at 1 GHz. For the L-band spectrometer/imager, spectra of standard samples showed that about 2×10^{14} nitroxide spins in water in an 8 mm o.d. tube using the 9-mm-diameter resonator could be detected with S/N ≈3 for 10 s signal averaging times that were used for the image projections and non-saturating B_1 of 5.6 μT. In multiple measurements of CP• and DCP• in the excised lungs, we measured about 2×10^{14} to about 1.5×10^{15} spins. Differences between male and female mice were not statistically significant (Fig. S1). Future studies will focus on the physiologic information obtained from imaging lungs from different strains of mice treated with LPS, compared with controls treated with PBS.

Several factors could potentially contribute to the differences in spin trapped radical intensity between CPH and DCP-AM-H shown in Fig. 4: (i) DCP-AM-H may react faster than CPH with superoxide, (ii) DCP• may be more resistant to bioreduction to diamagnetic products than CP•, or (iii) DCP• may accumulate in compartments where the concentrations of esterase and superoxide are high. We address each possibility in turn. The difference in signal intensity is unlikely to stem from differential reaction kinetics, since different cyclic hydroxylamines react with superoxide with comparable kinetics (e.g., the bimolecular rate constants for reaction of TEMPOL-H, 3CP-H, and CPH with superoxide are 2.1×10^3, 4.9×10^3, and 3.2×10^3 $M^{-1}s^{-1}$) [25, 26]. Bioreduction of the nitroxide product of the superoxide reaction cannot rationalize the differences in signal intensity, because DCP• is typically *more susceptible* to bioreduction than CP• [27], although the bioreduction may be dependent on the local environment [18].

Preferential compartmentalization of the probes involves two types of transport processes—passive partitioning of the hydroxylamine probes and the product nitroxides between the intracellular and extracellular compartments and active extrusion of the hydroxylamines and nitroxides out of the cell. Passive partitioning depends on the membrane permeability to a particular molecule, which is strongly correlated with the octanol/water partition coefficient of the molecule [28, 29]. For molecules like CPH, CP•, DCP-AM-H, and DCP•, the anionic (deprotonated) forms that predominate at physiological pH are essentially membrane-

impermeant, whereas the protonated (carboxylic acid) forms have measurable permeability. Thus, passive permeation of these species depends on the membrane permeability for the protonated forms and their pK_a values. Although the pK_a of DCP-AM-H has not been determined, pK_a estimation methods [30] suggest that the AM ester in DCP-AM-H lowers its pK_a by ~ 0.3 relative to CPH (i.e., at physiological pH, there is less of the protonated form of DCP-AM-H compared to CPH). On the other hand, the presence of the AM ester makes DCP-AM-H a little more lipophilic than CPH [31], and thus somewhat more membrane-permeant (although the effect is modest, because the AM ester is not as lipophilic as a simple methyl ester [31]). Since the pK_a and lipophilicity effects operate in opposite directions, the net result is that passive permeation is likely comparable for DCP-AM-H and CPH.

The major difference between DCP-AM-H and CPH is the presence of the AM ester, which is easily cleaved by abundant intracellular esterases [32–34]. Once the AM ester is cleaved, the resulting DCP-H and DCP• are both dicarboxylate ions at physiologic pH. This means that the diprotonated, membrane-permeant form is negligible and that DCP-H and DCP• are effectively trapped inside the cell. In contrast, CPH and CP• are mono-anions, whose protonated forms continue to allow passive permeation. An additional transport process is relevant. Organic anion transporters are ubiquitously expressed in mammalian cells and actively extrude xenobiotics [35]. We have shown that the rate of extrusion of organic ions is strongly dependent on the total charge on the ion [36]—the more highly charged the ion, the slower the extrusion. Our analysis show that single-charged ions are extruded almost 4-fold faster than double-charged ions [36]. Thus, AM ester cleavage produces a di-anion that loses the ability to leak out passively and is more resistant to active extrusion. Preferential intracellular accumulation of DCP-H and DCP• means that reaction with superoxide is enhanced (greater production of DCP•) and that the resulting EPR signal from DCP• is better retained in the cells of the tissue and not lost through wash-out.

Following future development of the 1 GHz spectrometer/imager, the goal is to perform measurements of the radicals in the lungs of live mice. Prior *in vivo* mouse studies have observed nitroxide radicals. Takeshita et al. injected 2.7×10^{18} spins intratracheally and measured the thorax of a mouse in a 33-mm i.d., 24-mm long, 1.3-GHz resonator [37]. A 34-mm diameter, 1.09 GHz resonator was used by Leonard et al. after injecting 3×10^{19} spins [38]. Caia et al. measured 5×10^{19} spins injected into a mouse contained in a 42-mm diameter, 1.2 GHz resonator [39]. Here, we can detect a smaller number of spins because the resonator is designed to match the sample. We construct the signal detection path to establish a low noise floor as close to the resonator as practical, and we use the revolutionary rapid scan method developed at the University of Denver. For nitroxide radicals in this type of sample, the rapid scan method provides about an order of magnitude increase in signal-to-noise for the same time as is achievable by CW EPR.

Summary

Based on treatment protocols developed using slices of lung tissue measured with an X-band spectrometer [8], we have imaged nitroxide radicals in intact excised lungs at 1 GHz. Sufficient radicals (2×10^{14} to 10^{15}) were present to enable 2D spectral-spatial imaging at

times up to several hours after sacrificing the mouse. Imaging was performed using the rapid scan EPR technique.

Supplementary Material

Refer to Web version on PubMed Central for supplementary material.

Funding

This work was supported in part by NIH NCI RO1CA1262159 (GRE) and R33 HL157907 (ESN and SSE).

Data Availability

Data are available from the authors on request.

References

1. Matthay MA, Zemans RL, Zimmerman GA et al. (2019) Acute respiratory distress syndrome. Nat Rev Dis Primers 5:18 [PubMed: 30872586]
2. Wang D, Hu B, Hu C et al. (2020) Clinicial Characteristics of 138 Hospitalized Patients with 2019 Noval coronavirus-infected pneumonia in Wuhan, China. J Amer Med Assoc 323:1061–1069
3. Channappanavar R, Perlman S (2017) Pathogenic human coronavirus infections: causes and consequences of cytokine storm and immunopathology. Semin Immunopathol 39:529–539 [PubMed: 28466096]
4. Calfee CS, Delucchi KL, Parsons PE, Thompson BT, Ware LB, Matthay MS (2014) Subphenotypes in acute respiratory distress syndrome: latent class analysis of data from two randomised controlled trials. Lancet Respir Med 2:611–620 [PubMed: 24853585]
5. Calfee CS, Delucchi KL, Sinha P et al. (2018) Acute respiratory distress syndrome subphenotypes and differential response to simvastatin: secondary analysis of a randomised controlled trial. Lancet Respir Med 6:691–698 [PubMed: 30078618]
6. Sinha P, Delucchi KL, Thompson BT, McAuley DF, Matthay MA, Calfee CS (2018) Latent class analysis of ARDS subphenotypes: a secondary analysis of the statins for acutely injured lungs from sepsis (SAILS) study. Intensive Care Med 44:1859–1869 [PubMed: 30291376]
7. Chow CW, Herrera AMT, Suzuki T, Downey GP (2003) Oxidative stress and acute lung injury. Am J Respir Cell Mol Biol 29:427–431 [PubMed: 14500253]
8. Elajaili HB, Dee NM, Dikalov SI, Kao JPY, Nozik ES (2023) Use of electron paramagnetic resonance (EPR) to evaluate redox status in a preclinical model of acute lung injury. Mol Imaging Biol 16:1–8
9. Sato K, Kadiiska MB, Ghio AJ et al. (2002) *In vivo* lipid-derived free radical formation by NADPH oxidase in acute lung injury induced by lipopolysaccharide: a model for ARDS. FASEB J 16:1713–1720 [PubMed: 12409313]
10. Li Y, Xiang M, Yuan Y et al. (2009) Hemorrhagic shock augments lung endothelial cell activation: role of temporal alterations of TLR4 and TLR2. Am J Physiol Regul Integr Comp Physiol 297:R1670–R1680 [PubMed: 19828841]
11. Mittal M, Siddiqui MR, Tran K, Reddy SP, Malik AB (2014) Reactive oxygen species in inflammation and tissue injury. Antioxid Redox Signal 20:1126–1167 [PubMed: 23991888]
12. Kellner M, Noonepalle S, Lu Q, Srivastava A, Zemskov E, Black SM (2017) ROS signaling in the pathogenesis of acute lung injury (ALI) and acute respiratory distress syndrome (ARDS). Adv Exp Med Biol 967:105–137 [PubMed: 29047084]
13. Bernardo ML, Lauterbur PC, Hedges LK (1985) Experimental example of NMR spectroscopic imaging by projection reconstruction involving an intrinsic frequency dimension. J Magn Reson 61:168–174

14. Maltempo MM, Eaton SS, Eaton GR (1987) Spectral-spatial two-dimensional EPR imaging. J Magn Reson 72:449–455
15. Eaton GR, Eaton SS, Ohno K (1991) EPR imaging and *in vivo* EPR. CRC Press, Boca Raton, FL
16. Eaton GR, Eaton SS (2022) Advances in rapid scan EPR spectroscopy. Method Enzymol 666:1–24
17. Eaton SS, Eaton GR (1990) Electron spin resonance imaging. In: Kevan L, Bowman M (eds) Modern Pulsed and Continuous Wave Electron Spin Resonance. Wiley Interscience, New York, pp 405–435
18. Dikalov SI, Dikalova AE, Morozov DA, Kirilyuk IA (2018) Cellular accumulation and antioxidant activity of acetoxymethoxycarbonyl pyrrolidine nitroxides. Free Radic Res 52:339–350 [PubMed: 29098905]
19. Buchanan LA, Rinard GA, Quine RW, Eaton SS, Eaton GR (2018) Tabletop 700 MHz EPR imaging spectrometer. Conc Magn Reson B Magn Reson Engin 48B:E21384
20. Stoll S, Schweiger A (2006) EasySpin, a comprehensive software package for spectral simulation and analysis in EPR. J Magn Reson 178:42–55 [PubMed: 16188474]
21. Rinard GA, Quine RW, Buchanan LA et al. (2017) Resonators for *in vivo* imaging: practical experience. Appl Magn Reson 48:1227–1247 [PubMed: 29391664]
22. Tseitlin M, Rinard GA, Quine RW, Eaton SS, Eaton GR (2011) Deconvolution of sinusoidal rapid EPR scans. J Magn Reson 208:279–283 [PubMed: 21163677]
23. Tseitlin M, Biller JR, Elajaili H et al. (2014) New spectral-spatial imaging algorithm for full EPR spectra of multiline nitroxides and pH sensitive trityl radicals. J Magn Reson 245:150–155 [PubMed: 25058914]
24. Eaton GR, Eaton SS, Barr DP, Weber RT (2010) Quantitative EPR. Springer-Verlag/Wien, New York
25. Zhang R, Goldstein S, Samuni A (1999) Kinetics of superoxide-induced exchange among nitroxide antioxidants and their oxidized and reduced forms. Free Radical Biol Med 26:1245–1252 [PubMed: 10381196]
26. Dikalov S, Skatchkov M, Bassenge E (1997) Spin trapping of superoxide radicals and peroxynitrite by 1-hydroxy-3-carboxy-pyrrolidine and 1-hydroxy-2,2,6,6-tetramethyl-4-oxo-piperidine and the stability of corresponding nitroxyl radicals towards biological reductants. Biochem Biophys Res Commun 231:701–704 [PubMed: 9070876]
27. Keana JF, Pou S, Rosen GM (1987) Nitroxides as potential contrast enhancing agents for MRI application: influence of structure on the rate of reduction by rat hepatocytes, whole liver homogenate, subcellular fractions, and ascorbate. Magn Reson Med 5:525–536 [PubMed: 3437813]
28. Levin VA, Dolginow D, Landahl HD, Yorke C, Csejtey J (1984) Relationship of octanol/water partition coefficient and molecular weight to cellular permeability and partitioning in s49 lymphoma cells. Pharm Res 1:259–266 [PubMed: 24277359]
29. Legenzov EA, Sims SJ, Dirda ND, Rosen GM, Kao JP (2015) Disulfide-linked dinitroxides for monitoring cellular thiol redox status through electron paramagnetic resonance spectroscopy. Biochemistry 54:6973–6982 [PubMed: 26523485]
30. Perrin DD, Dempsey B, Serjeant EP (1981) pKa prediction for organic acids and bases. Springer, Netherlands
31. Sano H, Naruse M, Matsumoto K-i, Oi T, Utsumi H (2000) A new nitroxyl-probe with high retention in the brain and its application for brain imaging. Free Radical Biol Med 28:959–969 [PubMed: 10802228]
32. Tsien RY (1981) A non-disruptive technique for loading calcium buffers and indicators into cells. Nature 290:527–528 [PubMed: 7219539]
33. Kao JP, Rosen GM (2004) Esterase-assisted accumulation of 3-carboxy-2,2,5,5-tetramethyl-1-pyrrolidinyloxyl into lymphocytes. Org Biomol Chem 2:99–102 [PubMed: 14737666]
34. Rosen GM, Burks SR, Kohr MJ, Kao JP (2005) Synthesis and biological testing of aminoxyls designed for long-term retention by living cells. Org Biomol Chem 3:645–648 [PubMed: 15703801]
35. Nigam SK, Bush KT, Martovetsky G et al. (2015) The organic anion transporter (OAT) family: a systems biology perspective. Physiol Rev 95:83–123 [PubMed: 25540139]

36. Legenzov EA, Muralidharan S, Woodcock LB et al. (2016) Designing molecular probes to prolong intracellular retention: application to nitroxide spin probes. Bioconjug Chem 27:2923–2930 [PubMed: 27998079]

37. Takeshita K, Hamada A, Utsumi H (1999) Mechanism related to reduction of radical in mouse lung using an L-band ESR spectrometer. Free Rad Biol Med 26:951–960 [PubMed: 10232839]

38. Leonard SS, Mowrey K, Pack D et al. (2002) In vivo bioassays of acute asbestosis and its correlation with EPR spectroscopy and imaging in redox status. Mol Cell Biochem 234(235):369–377 [PubMed: 12162455]

39. Caia G, Efimova OV, Velayutham M et al. (2012) Organ specific mapping of in vivo redox state in control and cigarette smoke-exposed mice using EPR/NMR co-imaging. J Magn Res 216:21–27

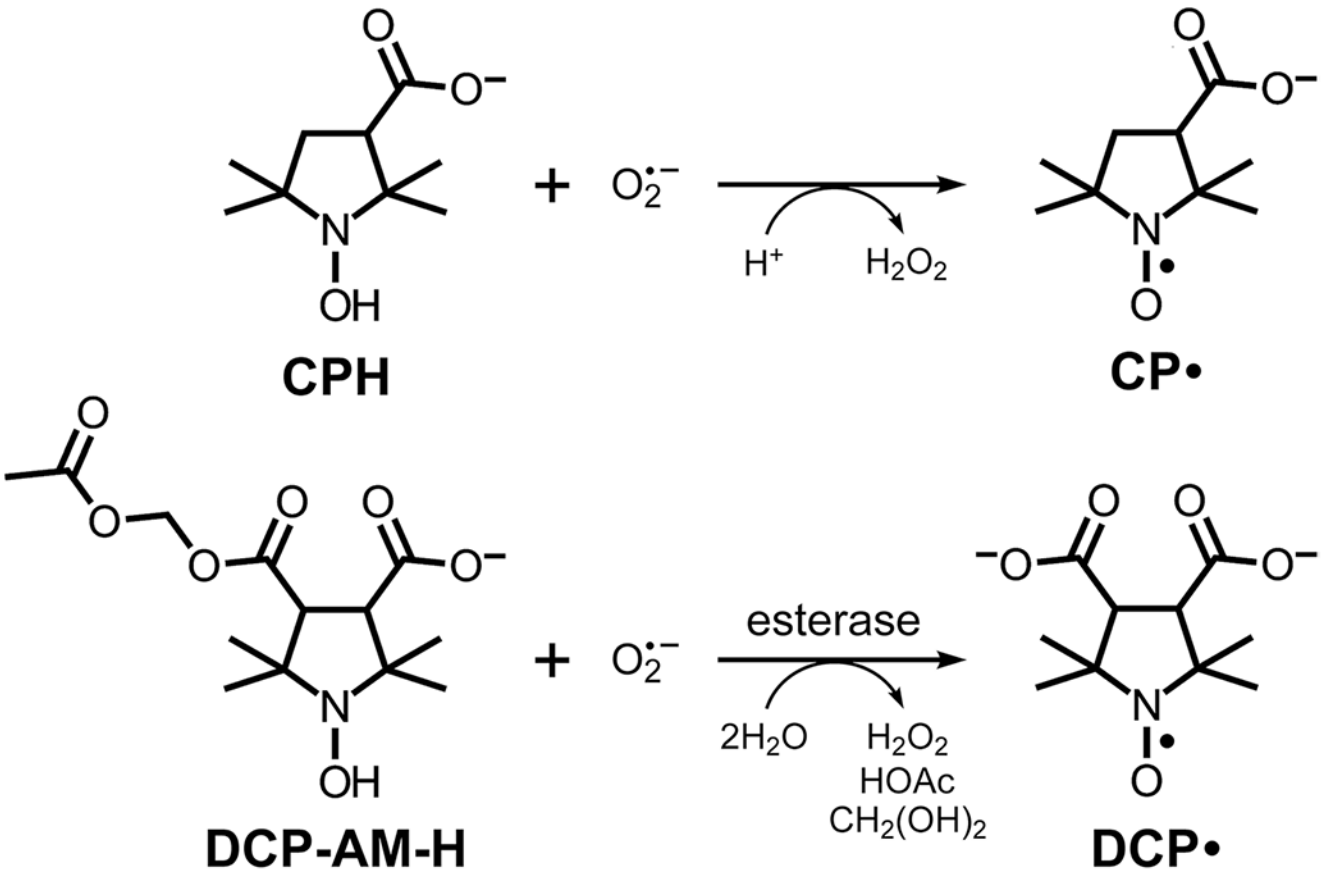

Fig. 1.

Structures of probes and products of reaction with superoxide. All carboxyl groups are shown in their deprotonated (anionic) forms, which are predominant at physiological pH

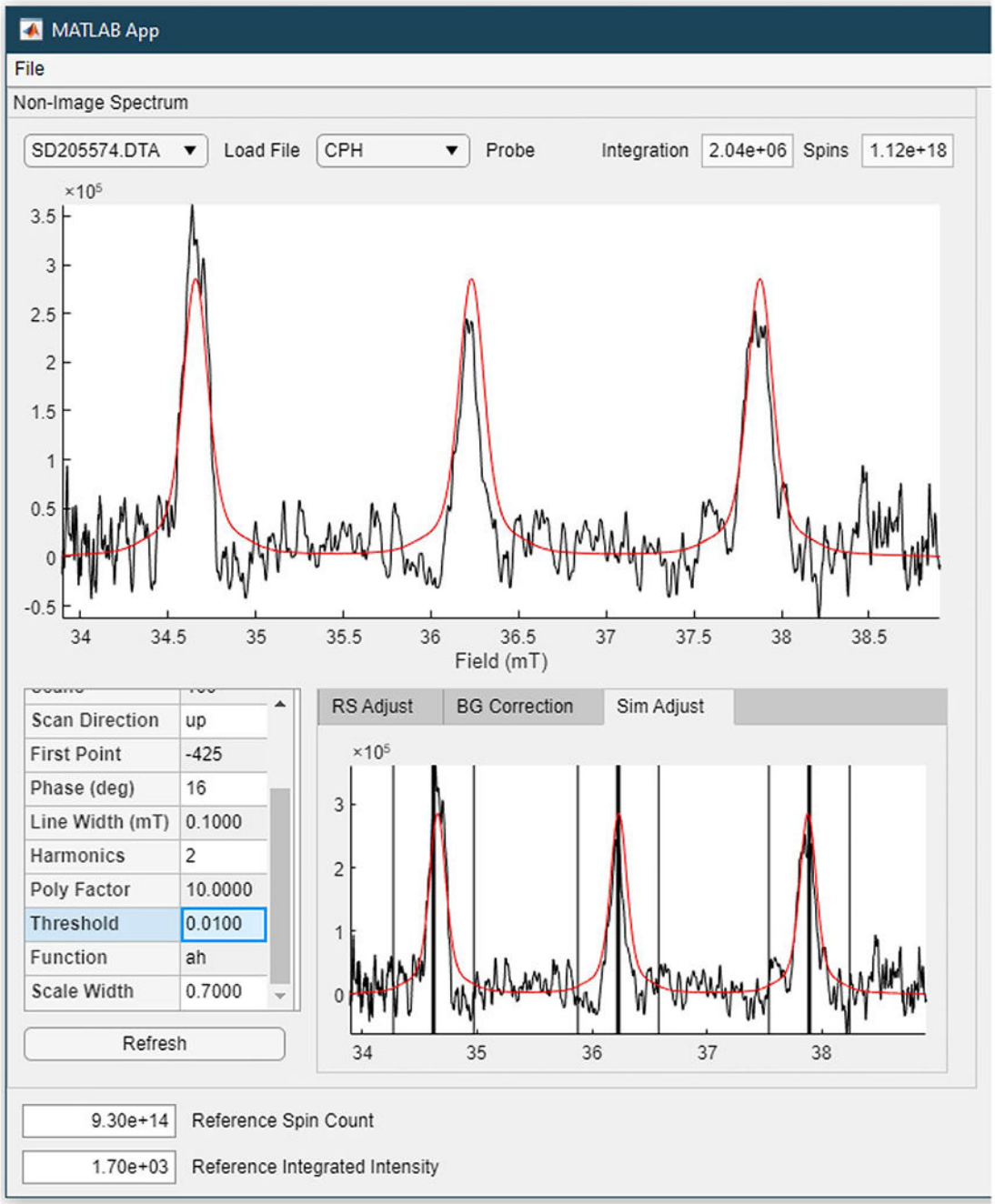

Fig. 2.

Screenshot of the output of the software used to simulate and quantitate spins in a spectrum or a spatial slice from an image. The EasySpin rescale routine is used to calculate the scaling of the reference spectrum to the experimental data within the 3 selected windows centered on the positions of the three lines in the nitroxide spectrum

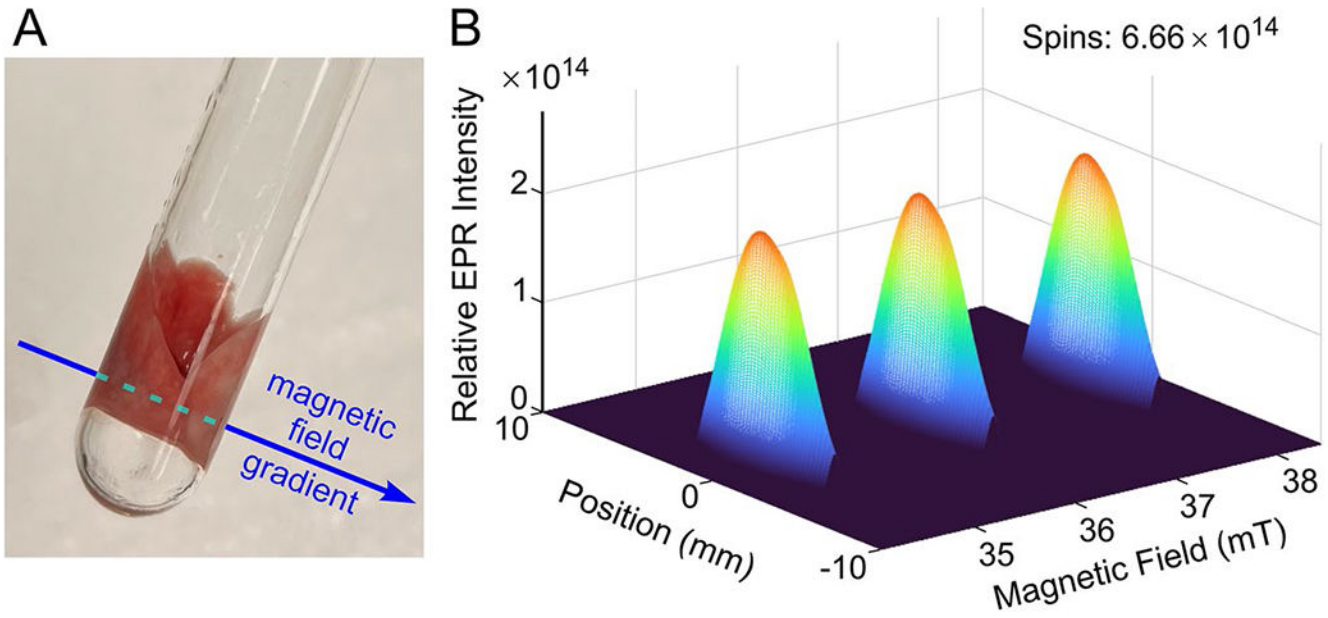

Fig. 3.

Sample and gradient geometry for the acquisition of EPR spectral-spatial images of excised lungs. **a** Excised mouse lungs in an NMR tube (8 mm o.d., 7 mm i.d.). An applied magnetic field gradient defines the spatial axis. **b** 2D spectral-spatial image displaying the full EPR line shape as a function of position along the spatial axis defined by the direction of the magnetic field gradient. The EPR spectrum is the 3-line nitroxide signal from CP• in the lungs from an LPS-treated mouse

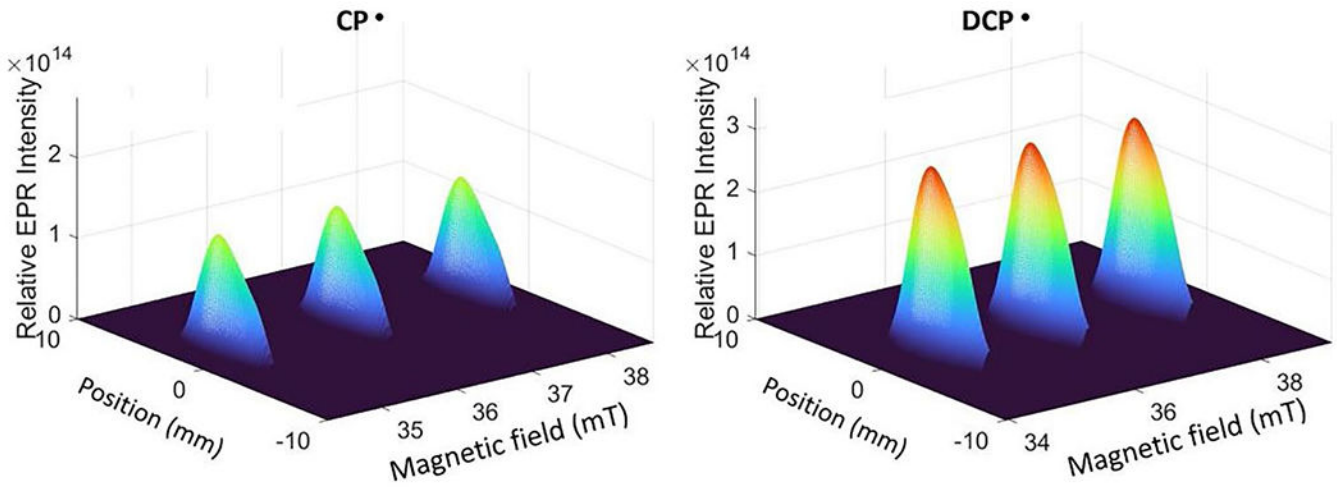

Fig. 4.

Spectral-spatial images of the signals from CP• or DCP• in the lungs of LPS-treated mouse that contained $(4.5 \pm 0.5) \times 10^{14}$ and $(9.9 \pm 1) \times 10^{14}$ nitroxide spins, respectively